Structural evolution-enabled $BiFeO_3$ modulated by strontium doping with enhanced dielectric, optical and superparamagnetic properties by a modified sol-gel method

Sharon V S, Veena Gopalan E, and Malini K A[†]

Department of Physics Vimala College Thrissur-9, Kerala, India

(Received 12 February 2022; revised manuscript received 4 June 2022; accepted manuscript online 14 June 2022)

Multiferroic (BFO) nanoparticles doped with strontium with the general formula $Bi_{1-x}Sr_xFeO_3$ ($x = 0$, 0.3, 0.5, 0.7) were synthesized using a modified sol-gel auto-combustion process. The structural, electrical, optical, and magnetic properties of the samples are discussed. The structural analysis, carried out using the x-ray powder diffraction technique, shows a structural transition from rhombohedral (R-3c) to cubic (Pm-3m) for the doping amount of strontium (Sr) equal to $x = 0.3$. Morphological analysis of the prepared samples were carried out using scanning electron microscopy (SEM). Frequency-dependent dielectric constant and ac conductivity were studied. The doped samples, with improved dielectric properties, can be used to fabricate different optoelectronic devices. Strong dielectric dispersion and broad relaxation were exhibited by all the samples. Cole–Cole plots were employed as an effective tool to study the dispersion parameters, namely, the optical dielectric constant, static dielectric constant, relaxation time, and spreading factor. The activation energy was calculated from the relaxation peaks and Cole–Cole plots, which were found to be compatible with each other. The bandgap of the samples was calculated using diffuse reflectance spectral (DRS) analysis. Sharp and strong photoluminescence in the IR region was observed in the samples, similar to ZnO, which was reported for the first time. Room-temperature and low-temperature magnetization studies point towards the superparamagnetic nature of the samples, with an improvement in magnetic properties with doping. The antiferromagnetic behavior of bulk bismuth ferrite transforms to superparamagnetic in nature for both pure and Sr-substituted bismuth ferrite nanoparticles due to the close dimensions of crystallite size with magnetic domains leading to the break-down of the frustrated spin cycloidal moment.

Keywords: multiferroics, sol-gel process, x-ray spectra, optical and dielectric properties

PACS: 75.85.+t, 95.30.Dr **DOI:** 10.1088/1674-1056/ac785b

1. Introduction

Multiferroics, also known as magneto electrics, possess more than one ferroic or anti-ferroic property in a single material, e.g., ferromagnetic, ferroelastic, ferroelectric, etc., and their ferroic properties are coupled with each other.[1] They find numerous applications in spin valves, spintronics, data storage, microelectronic devices, quantum electromagnets, etc.[2,3] The disagreement between the emergence of different ferroic orders limits the formation of single-phase multiferroic materials. The existence of d-electrons for magnetism is not congenial with the off-center movement of cations responsible for ferroelectricity, which entails empty d-orbitals.[4] Bismuth ferrite (BFO) is an environmentally friendly material and is an interesting member of the multiferroic family in which both ferroelectricity and anti-ferromagnetism coexist.[5] $BiFeO_3$ (BFO) has a rhombohedral distorted perovskite structure, with the space group $R3c$ at room temperature.[6] Pure BFO has high conductivity and an antiferromagnetic nature because of charge defects.[7] Pure bismuth ferrite has weak magnetoelectricity due to its spatial periodic nonhomogeneous spin structure, which limits its application in various devices; hence, the addition of dopants can enhance its utility.[8] The magnetic and structural properties of $BiFeO_3$ nanoparticles greatly depend on the doping, particle size, pressure, morphology, etc., which can be controlled by the synthesis procedure. Hence, the preparation method has a pronounced effect on the magnetic and structural properties of $BiFeO_3$ nanoparticles.

Many reports have demonstrated that suitable alkaline earth metal substitution in BFO could significantly improve its physical properties. Hence, one can improve the properties of BFO by cation substitution at the Bi site. Ions of rare earth metals and alkaline earth metals (Mg, Ca, Ba, Sr, etc) have been used by many researchers to improve the multiferroic properties of BFO.[9,10] Due to the closeness in the ionic radius of strontium (1.18 Å) with bismuth (1.03 Å), Sr is the best choice of substitution at the bismuth site. From this substitution, a charge imbalance would be created that could be compensated in 3 ways: (i) creation of oxygen vacancies, (ii) charge discrepancy of Fe^{3+} and Fe^{5+}, and (iii) partial transformation of Fe^{3+} to Fe^{4+}.[9] The preparation of pure BFO without impurities is very difficult. Recently, the optical properties of $BiFeO_3$ have also been studied in a limited wavelength range by several researchers.[11,12] There are also studies that have been performed to prepare nanostructures of $BiFeO_3$ with different optical properties resulting from quantum confinement.[11] Only a few articles have reported

[†]Corresponding author. E-mail: malinijayram@vimalacollege.edu.in

© 2023 Chinese Physical Society and IOP Publishing Ltd

the possible application of $BiFeO_3$ in optoelectronic devices in the visible region.[12] In this paper, we report the synthesis of Sr-doped bismuth ferrite with the composition $Bi_{1-x}Sr_xFeO_3$ ($x = 0$, 0.3, 0.5, 0.7) using a modified sol-gel method. The advantage of this method is that it is an easy and cost-effective technique to yield homogenous and ultrafine powder. The prepared samples are labeled as BFO, BSFO-0.3, BSFO-0.5, and BSFO-0.7, respectively. The structural, dielectric, optical, and magnetic properties of the samples are evaluated. The trivalent bismuth sites, when substituted by divalent strontium ions, are expected to create charge imbalance and oxygen vacancies in the doped samples.[9] In this work, the effect of divalent doping on the photoluminescence properties of BFO is reported. The studies indicate the superparamagnetic behavior and significant previously unreported luminescence properties in the IR region for Sr-doped bismuth ferrite nanoparticles.

2. Experimental details

2.1. Material synthesis

BFO nanoparticles and strontium-doped bismuth ferrite nanoparticles (BSFO) ($Bi_{1-x}Sr_xFeO_3$ ($x = 0$, 0.3, 0.5, 0.7)) were synthesized using a modified sol-gel auto-combustion method. The precursors used for the synthesis of $Bi_{1-x}Sr_xFeO_3$ nanoparticles were analytical grade bismuth nitrate, strontium nitrate, iron nitrate, and citric acid of purity $\sim 98\%$ purchased from Merck. The stoichiometric amount of metal nitrates was weighed and dissolved separately in deionized water to obtain the respective solution. Citric acid was added to the metal nitrate solution in the molar ratio of 1:1. The typical synthesis procedure for BSFO-0.5 requires an analytical grade of 0.5 M bismuth nitrate, 0.5 M strontium nitrate, 2 M iron nitrate, and 3 M citric acid solutions, respectively. The solutions were then mixed and heated at 80 °C for 30 min with constant stirring. Then, it was shifted to a hot plate and evaporated at an elevated temperature to form a dark viscous resin. Continuous heating leads to the auto-combustion of resin, and brown-colored samples were obtained after combustion. The other compositions were also prepared by using precursor solutions of appropriate molarity. The impurity content was minimized by the leaching of nitric acid and by washing the samples several times with distilled water.

2.2. Characterization

The prepared samples were characterized by XRD on a Brucker AXS D8 x-ray diffractometer using Cu-$K\alpha$ radiation. The crystalline size was calculated from the Scherrer formula. The prepared powder samples were mixed with 3% PVA and pressed into pellets of 12 mm diameter by a hydraulic press at a pressure of 0.53 ± 0.003 MPa for 3 min. Then, the pellets were sintered at 900 °C for 4 hours for the dielectric measurements. The frequency variation of the dielectric constant and conductivity of the samples were studied using an HP 4285 LCR meter at room temperature in the frequency variation of 100 kHz–5 MHz. DRS analysis was carried out using a Shimadzu UV-Vis spectrophotometer (UV-2600). The photoluminescence spectrum was recorded using a Shimadzu Spectrofluorophotometer (RF5301 PC). The magnetic properties were measured using a VSM (SQU, Sultanate of Oman) at room temperature (300 K) and low temperature (5 K).

3. Results and discussion

3.1. Structural studies

The XRD patterns of all the prepared samples are shown in Fig. 1. The most intense peaks were matched with the PCPDF file (86-1518). The XRD pattern confirms the formation of a rhombohedral perovskite *R*-3*c* structure related to bismuth ferrite. The secondary phase of bismuth ferrite $Bi_2Fe_4O_9$ also appeared. The result is in very good agreement with the previously reported paper.[9] The x-ray diffractograms reveal that for samples $x = 0.3$ and 0.5, two peaks are merged into one single peak, indicating that the crystal structures of BSFO-0.3 and BSFO-0.5 have been transformed from rhombohedral to the cubic phase (space group, *Pm*-3*m*), which agrees with the previously reported results.[13] This may be due to the presence of the Sr^{2+} cation that compensates for the evaporation of the Bi^{3+} cation during the preparation (*Pm*-3*m*). The XRD pattern of BSFO-0.7 in Fig. 1 reveals that all the peaks are indexed to the cubic space with the *Fd*-3*m* space group. The diffraction peaks correspond to the (220), (311), (400), (422), (511), and (440) crystal planes exhibited by the face-centered cubic crystal and are in good agreement with JCPDS-00-001-1121. The Bi^{3+} ions contain $6s^2$ lone pair electrons (Bi:[Xe] $4f^{14}5d^{10}6s^26p^3$). The existence of this highly polarized lone pair in bismuth ferrite is behind the displacement of Bi^{3+} from its centrosymmetric position, causing the formation of a rhombohedral structure with the space group *R*-3*c*. With the existence of Sr^{2+} ions, this polar displacement can be suppressed by the emergence of oxygen vacancies, whereby the lone pair electron goes directly into the space of the vacancies. This leads to the development of a more symmetric environment around Bi^{3+}, leading to the cubic structure (*Pm*-3*m*).[14]

The average crystallite sizes of the samples were obtained using Scherrer's formula.[9] The crystallite size was calculated for the samples BFO, BSFO-0.3, BSFO-0.5, and BSFO-0.7 were 48.39 nm, 10.03 nm, 13.23 nm, and 13.10 nm, respectively. From the XRD pattern, lattice parameters for the prepared samples were also calculated and are given in Table 1. Figure 2 shows the XRD pattern of all the samples fired at 790 °C for 1 hour. The XRD pattern in Fig. 2 confirms the formation of $Bi_{24}(Bi_{1.04}Fe_{0.84})O_{40}$, bismuth iron oxide (PCPDF 82-1316). This indicates that one can obtain good

quality bismuth ferrite nanoparticles via the modified sol-gel method, which is a considerably less expensive, simple, and fast method compared to a high-temperature synthesis.

Table 1. The space group, lattice parameters and volume for all the doped and undoped samples.

x	0	0.3	0.5	0.7
Space group	*R*-3*c*	*Pm*-3*m*	*Pm*-3*m*	*Fd*-3*m*
$a = b$ (Å)	5.51	3.97	3.97	8.38
c (Å)	13.8	3.97	3.97	8.38
V (Å^3)	362.03	62.57	62.57	588.48

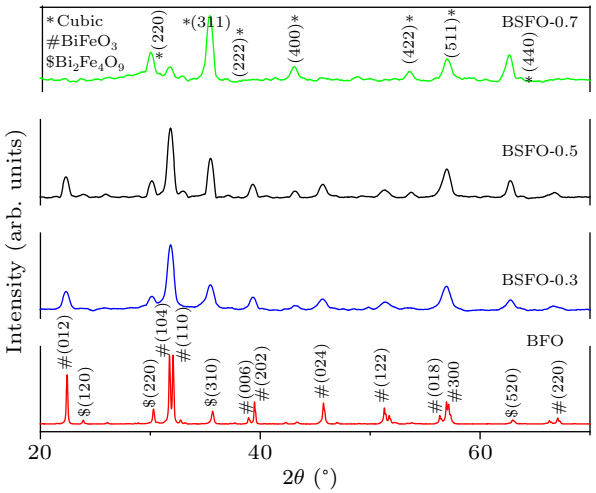


Fig. 1. X-ray diffractograms of all the samples.

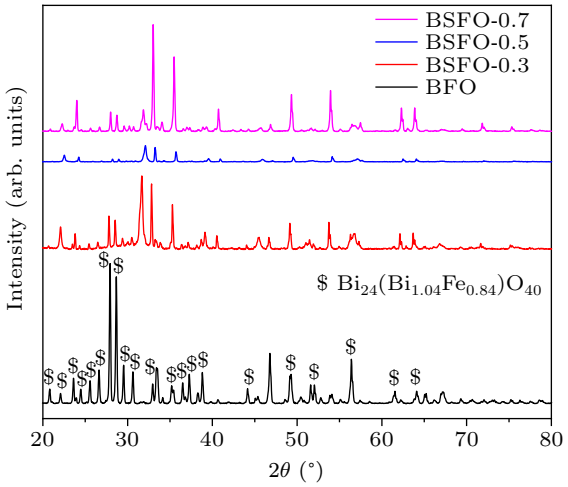


Fig. 2. X-ray diffractograms of all the samples sintered at 790 °C.

3.2. Microstructure characterization

The morphology of the BSFO-0.5 nanoparticles was analyzed using a high-resolution scanning electron microscope (SEM). The SEM provides information about the surface morphology of the $Bi_{0.5}Sr_{0.5}FeO_3$ nanoparticles. Figure 3 displays the SEM images of the BSFO-0.5 nanoparticles, and shows undesirable grown nanoparticles. This may be caused by excessive Sr doping.[13]

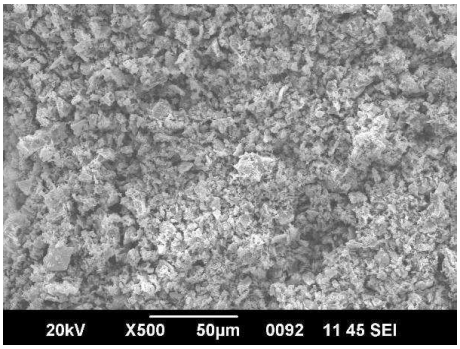


Fig. 3. An SEM image of the BSFO-0.5 nanoparticles.

3.3. Dielectric studies

The dielectric constant is evaluated using the relation

$$\varepsilon = \frac{Cd}{\varepsilon_0 A}, \tag{1}$$

where C is the equivalent parallel capacitance, d is the thickness of the pellet, ε is the permittivity of free space and A is the area of the disc. Cole–Cole plots were drawn using the circle least squares method, making use of real and imaginary values of dielectric permittivity[15] to obtain the dispersion parameters. The loss factor or dissipation factor in any dielectric is specified by the expression

$$\tan\delta = \frac{\varepsilon''(\omega)}{\varepsilon'(\omega)}, \tag{2}$$

where ε' and ε'' are the real and imaginary parts of the complex dielectric permittivity.

3.3.1. Dielectric dispersion

The variation of the dielectric constant with frequency for the prepared samples is given in Fig. 4. It is observed that the dielectric constant decreases with increasing frequency; the decrement in the dielectric constant is due to dielectric relaxation. According to Koop's theory, dielectric material has a double layer structure with one conducting and one insulating layer. According to the theory, dielectric relaxation is due to orientational polarization.

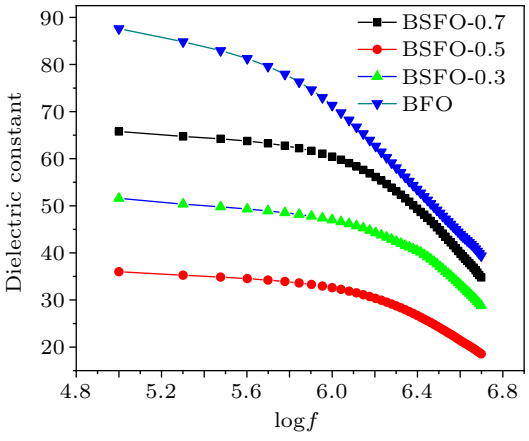


Fig. 4. Variations in the dielectric constant with frequency.

The relaxation time is the time taken by the dielectric materials to align themselves in the direction of the external electric field.[16] Each dielectric material needs a finite time to align with its axis along the applied electric field. As the frequency increases, a point is reached when the charge carriers do not align with the applied external electric field; therefore, polarization cannot reach the saturation value and also does not follow the alternating electric field. This is the reason for the fast decrease in the dielectric constant with frequency at larger frequencies.[9] In this work, the maximum observed value of the dielectric constant at low frequency is greater than the reported value of Sr-doped bismuth ferrite.[9] All the samples have a high dielectric constant value (~ 50), and hence are used in gate dielectrics and photoelectrochemical cells. Thus, these materials are important for technological applications.[17]

Figure 5 shows the variation in the dielectric constant with temperature for BFO. An almost constant dielectric constant value is found at lower temperatures as the dipole molecules cannot orient themselves in this region.[18] As the temperature increases the orientation of interface dipoles increases, and hence dielectric permittivity increases. As the temperature increases, the accumulation of charge on the grain boundaries increases, which in turn increases the interfacial polarization and hence the dielectric constant.[19]

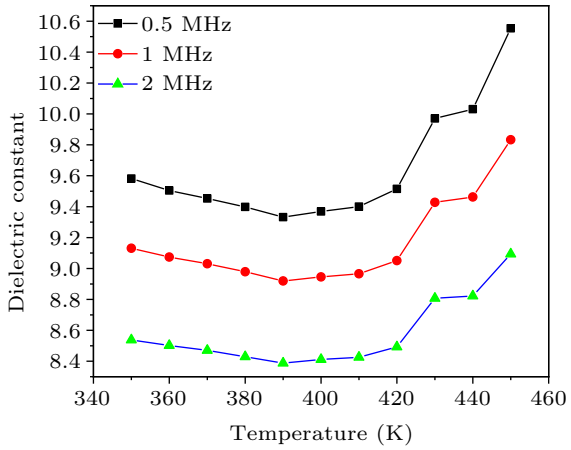


Fig. 5. Dielectric permittivity as a function of temperature.

3.3.2. Dielectric absorption

Dielectric absorption in a material is specified by $\tan\delta$ values. It can be noted that $\tan\delta$ values, when plotted against frequency, reveal relaxations at specified frequencies (Fig. 6). Dielectric relaxation takes place when the hopping frequency of charge carriers is equal to the applied field frequency.[20]

However, it is to be noted that better relaxation can be observed in the sample with $x = 0.7$; this may be due to promotion in several hopping charges available for $x = 0.7$. Also, for $x = 0.7$, the sample has the properties closest to the cubic structure. This behavior also confirms the probable structural change in BSFO-0.7. The relaxation peaks corresponding to other compositions lie outside the frequency range of measurement.[19]

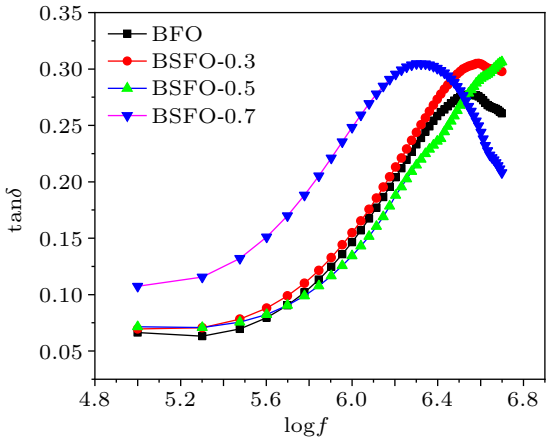


Fig. 6. The tanδ value with frequency of all the samples.

3.3.3. Variation of ac conductivity

The variation in ac conductivity with frequency was also studied for all the samples and is plotted in Fig. 7.

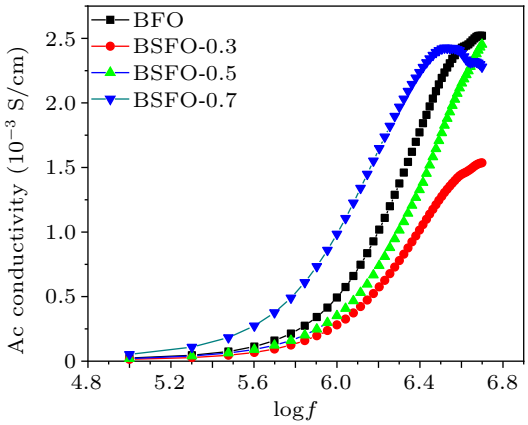


Fig. 7. The dependence of ac conductivity on frequency of all the samples.

It is observed that conductivity increases with increasing frequency. This is connected to the hopping of electrons from Fe^{2+} to Fe^{3+} ions. The decreasing dielectric constant with frequency is also associated with the hopping of electrons from Fe^{2+} to Fe^{3+} ions. The hopping electrons need a large amount of energy. At low frequency these electrons could not get sufficient energy from the electric field but, as we increase the frequency of the electric field, the electrons get sufficient energy and, at a particular point, the hopping of electrons begins from Fe^{2+} to Fe^{3+}. This is why the conductivity of dielectric material increases with increasing frequency and the decrement in the dielectric constant.

3.3.4. Effect of strontium substitution on dielectric properties

The variations in the dielectric constant and conductivity with Sr content for the prepared samples are plotted in Figs. 8 and 9.

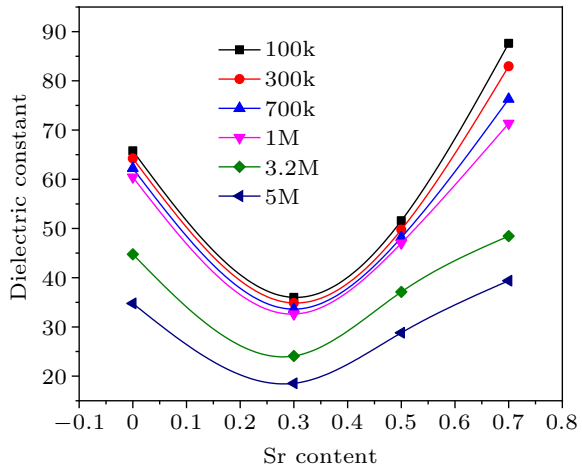


Fig. 8. Variation of the dielectric constant with Sr content in BFO.

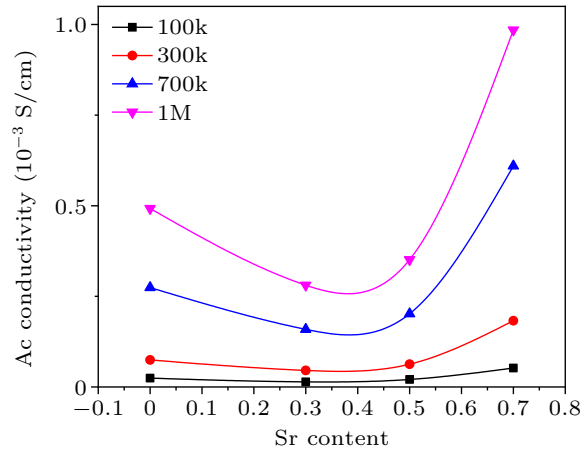


Fig. 9. Variation of ac conductivity with Sr content in BFO.

The decreasing dielectric constant ($x = 0.3$) may be due to two phenomena. The substitution of Sr ions in BFO introduces more oxygen vacancies due to charge compensation, which increases the hopping conduction mechanism. Second, this may be due to the substitution of higher radii strontium ions and the presence of traces of a secondary phase, which reduces grain sizes (increased grain boundaries), and the inhomogeneity, which gives restriction to the charge movement. Strontium substitution has a considerable effect on the dielectric properties of BSFO.[21]

Doping with more strontium increases the dielectric constant ($x \sim 0.3$) due to leakage current. The high conductivity and leakage current are caused by the part of the impurity phase, so that even a very small number of impurities separated to the boundaries can have a doping effect and change the dielectric to a semiconductor.[22] In pure BFO samples, the spontaneous change in the oxidation state from Fe^{3+} to Fe^{2+} results in the formation of oxygen vacancies to maintain the electrical neutrality, which causes thermally activated hopping conduction. In our samples, the presence of oxygen vacancies contributes to the increase in conductivity ($0.3 < x < 0.7$); when $0 < x \leq 0.3$ the Fe^{3+} ions become donors and the number of Fe^{2+} ions that change from Fe^{3+} become less, which reduces the conductivity. Doping with $x = 0.5, 0.7$ increases the conductivity and hence the dielectric constant due to structural transition. By doping, we can modify the dielectric properties to suit application requirements.[23] The measurement of the dielectric constant and ac conductivity of BSFO samples suggests that the leakage current plays an important role.[24]

Figure 6 shows the effect of Sr substitution on the tanδ of the BSFO series. An enlarged dielectric absorption value is seen with an increase in strontium concentration. Doping with strontium $x = 0.7$ increases the conductivity and leakage current due to the structural transition. The dielectric polarization is based on the hopping of charge carriers. Relaxation takes place when the hopping frequency equals the applied frequency.

3.3.5. Cole–Cole representation of dielectric data

The Debye equation for dielectric dispersion is given by

$$\varepsilon^* - \varepsilon_\infty = \frac{(\varepsilon_s - \varepsilon_\infty)}{(1 + j\omega\tau)}, \tag{3}$$

where ε^* is the complex permittivity, ε_s and ε_∞ are the values at limiting frequencies, i.e., the static dielectric constant and optical dielectric constant, $\omega = 2\pi f_{max}$ and τ is the relaxation time. The Cole–Cole plots in this case are semicircular with a center on the real axis. In those materials that possess dielectric dispersion, a variation from ideal Debye behavior is observed, as there is the possibility of the existence of multiple relaxation times.[25–27] K S Cole and R H Cole suggested that in such cases, permittivity follows the empirical equation

$$\varepsilon^* - \varepsilon_\alpha = \frac{(\varepsilon_s - \varepsilon_\alpha)}{1 + (j\omega\tau_0)^{1-\alpha}}, \tag{4}$$

where τ is the average relaxation time and α is the spreading factor of the actual relaxation time τ about its mean value τ and α lies in the range 0–1. A plot of ε'' for a certain frequency against ε' at the same frequency in the complex plane is represented as a Cole–Cole plot. For $\alpha = 0$, the above equation reduces to Debye's equation; for a dielectric with $\alpha = 0$ or single relaxation time, the Cole–Cole plot is a semicircle; and for $\alpha \sim 0$, the plot is a circular arc with its center lying below the real axis. The spreading factor α can be calculated from the expression for a maximum value of the imaginary part of the permittivity

$$\varepsilon''_{max} = \frac{(\varepsilon_s - \varepsilon_\infty)(\tan[(1-\alpha)\pi/4])}{2}. \tag{5}$$

The average value of τ can be calculated from the equation

$$\frac{(\varepsilon_0 - \varepsilon')^2 + \varepsilon''^2}{(\varepsilon' - \varepsilon_\infty)^2 + \varepsilon''^2} = (j\omega\tau_0)^{2(1-\alpha)}. \tag{6}$$

The molecular relaxation time calculated using the equation by substituting the value of τ_0 is

$$\tau = [(2\varepsilon_s + \varepsilon_\infty)/3\varepsilon_s]\tau_0. \tag{7}$$

A detailed description of these derivations is given elsewhere.[27]

The Cole–Cole plots corresponding to the samples are plotted in Fig. 10. The dispersion parameters, i.e., static dielectric constant ε_s, optical dielectric constant ε_α, spreading factor α, average relaxation time τ_0, and molecular relaxation time τ, of all the samples are evaluated and tabulated and their variation with composition is analyzed (Fig. 11). The values of the dispersion parameters obtained from the Cole–Cole plot analysis are given in Table 2.

Table 2. Dispersion parameters from the Cole–Cole analysis.

Sr content in sample (x)	ε_s	ε_∞	A	ε''	τ_0 (10^{-8} s)	τ (10^{-8} s)
0	67.352	28.611	0.256	12.802	1.12	0.912
0.3	36.739	14.293	0.263	7.335	0.994	0.791
0.5	52.547	19.835	0.299	10.029	0.795	0.630
0.7	92.733	35.369	0.280	18.177	1.92	1.53

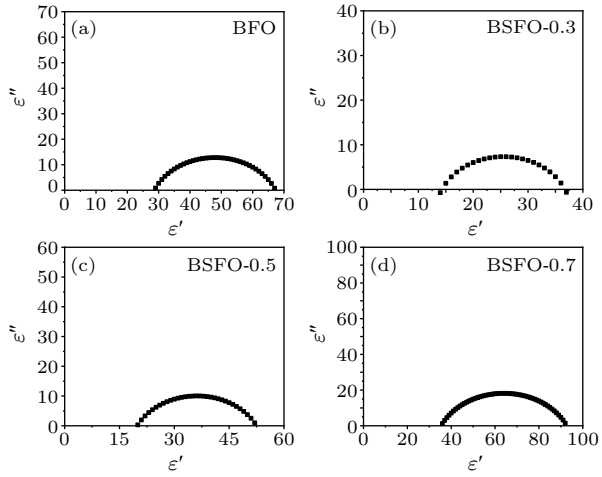


Fig. 10. Cole–Cole plots of all the samples.

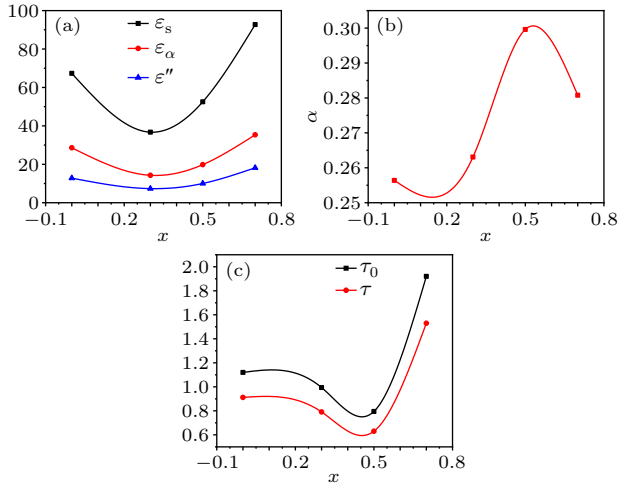


Fig. 11. The static dielectric constant ε_s, optical dielectric constant ε_α, spreading factor α, average relaxation time τ_0, and molecular relaxation time τ of all the samples.

The optical dielectric constant (ε_α) and static dielectric constant (ε_s) are initially decreased for $x = 0.3$ and further addition of strontium increases their values, which is similar to that in Fig. 8. This is because the dielectric constant of a material is linearly proportional to the average value of the grain size.[28] Therefore, the decrease in the dielectric constant for $x = 0.3$ is due to a decrease in grain size. For $x = 0.5$ and 0.7, the grain size and the dielectric constant increase. This indicates that there is a relation between the conduction process, dielectric polarization, and the grain size in Sr-doped BFO samples. The grain boundary mobility decreases with Sr doping due to the segregation at the grain boundaries of defects induced by doping.[28] The spreading factor is the measure of the broadening of the relaxation time. The average relaxation time is the effectual time constant for the relaxation involved, and the molecular relaxation time is the time constant for the instantaneous molecular dipole relaxation.[19] The spreading factor increases with Sr doping up to $x = 0.5$, which may be attributed to the increase in disordering in BSFO nanoparticles as a result of doping. It is clear from the table that the relaxation time (i.e., average and molecular) decreases up to $x = 0.5$ and increases to $x = 0.7$. This may be because, by increasing doping up to $x = 0.5$, disorders in the nanoparticles increase, thereby decreasing the relaxation time. In the sample $x = 0.7$, the spreading factor decreases and the relaxation time increases because the disorder in the structure decreases, and there is also a structural transition from *Pm*-3*m* to *Fd*-3*m*.[29]

The ambiance for observing a maximum dielectric loss of a dielectric material is given by the relation $\omega\tau' = 1$, where τ' is the relaxation time and $\omega = 2\pi f_{\max}$.

The relaxation time can be written as

$$\tau' = \tau_0 \exp\left(\frac{E_d}{k_B T}\right), \tag{8}$$

where τ is the pre-exponential factor, which is equal to the relaxation at infinite temperature, k_B is the Boltzman's constant, T is the absolute temperature and E_d is the activation energy for dielectric relaxation. It is clear from this relation that, as the temperature increases, relaxation time decreases. The activation energy for dielectric relaxation was calculated from the slope of the ln τ versus $1000/T$ (Fig. 12). The calculated activation energy for $BiFeO_3$ is found to be 0.240 eV. This value is close to the reported values.[30]

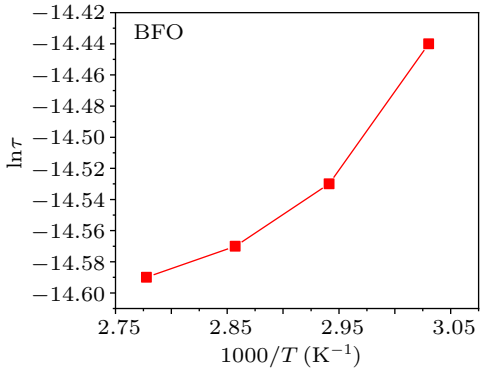


Fig. 12. The ln τ versus $1000/T$.

4. Optical studies

BFO shows optical properties that can be used in photoconductive and photocatalytic applications. Optical studies are mainly based on UV-visible absorption spectra and photoluminescence studies. Figure 13 shows UV-visible absorption spectra at room temperature for all the samples in the spectral range 1.5 eV–2.75 eV.

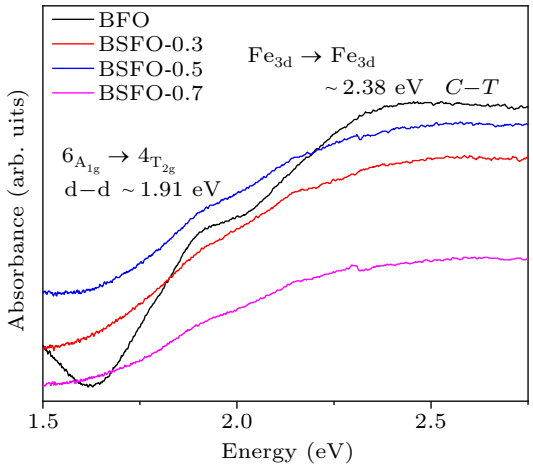


Fig. 13. UV-visible absorption spectra for all the samples.

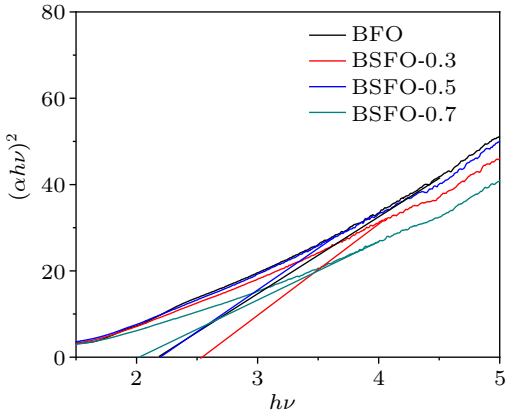


Fig. 14. Tauc's plot to determine the band gap of all the samples.

A band corresponding to 1.91 eV has been observed, which corresponds to the d–d transition of Fe_3P ions as degenerate d orbitals undergo splitting due to interaction with ligands. In the literature, these transitions are marked as theoretically forbidden excitations. These bands show a small intensity and the relaxation is due to spin–orbit coupling.[31] The absorption increases up to 2.5 eV and then shows broadband due to charge transfer (CT). The CT band around 2.5 eV is attributed to $Fe_1$3d–$Fe_2$3d inter-site electron transfer.[32] The small changes in the in d–d and charge transfer bands with Sr doping may be attributed to the stress due to the change in volume produced by the substitution of larger Sr ions.[33] The energy bandgap (E_g) plays an important role in the semiconductor of BFO, which can be calculated from absorption spectra. The direct bandgap can be calculated from the classical Tauc's law[34]

$$\alpha h\nu = A(h\nu - E_g)^{1/2}, \tag{9}$$

where $h\nu$ is the photon energy, h is Planck's constant, α is the absorption coefficient, E_g is the optical energy gap, and A is the constant function. When we plot a graph between $(\alpha h\nu)^2$ versus $h\nu$, the extrapolation of the straight line to the $(\alpha h\nu)^2 = 0$ axis gives the energy gap. The Tauc plot for the samples is shown in Fig. 14.

The optical band gap was calculated to be 2.19 eV, 2.54 eV, 2.22 eV, and 2.04 eV, respectively, for samples with $x = 0$, 0.3, 0.5, and 0.7. The calculated band gap of bismuth ferrite is in very good agreement with previously reported studies.[35] The decrease in the bandgap is due to the orientation of the oxygen octahedral and the structural transition of the samples. The lower bandgap and larger absorption in the BFO system is important for multiferroic semiconductors, photocatalytic applications, and hydrogen generation through photocatalytic water splitting.[11,36]

The photoluminescent (PL) emission spectrum of the as-prepared samples is shown in Fig. 15. It presents the luminescent response of bismuth ferrite and doped samples. The emission peaks are observed at 863 nm, 842 nm, 858 nm, and 730 nm for the samples $x = 0$, 0.3, 0.5, and 0.7, respectively, for excitation wavelengths of 570 nm, 422 nm, 430 nm, and 366 nm.

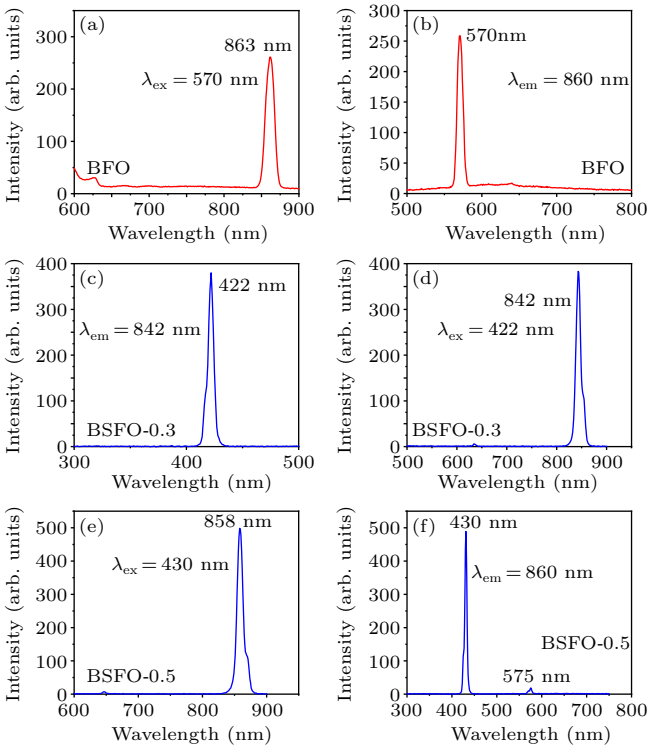


Fig. 15. Deconvoluted peak profiles for the PL spectrum $BiFeO_3$, $Bi_{0.7}Sr_{0.3}FeO_3$, and $Bi_{0.5}Sr_{0.5}FeO_3$.

The emission spectrum greater than 780 nm is in the infrared region. Optical properties evaluation helps to determine its usefulness in photoconductive and photocatalytic

applications.[11] Most of the optical studies that have reported on BFO-based systems have been based on UV-vis or limited optical range PL studies. But there is no detailed PL study in the IR region of the spectrum. This range is interesting because of O-vacancies-induced luminescence.[37] Strong luminescence lines are found in the IR region for all the samples due to the O vacancies. The wavelength around this region can be used for optical communication.[38] A systematic study in the lines in the IR region may lead to some interesting application possibilities for these materials.

4.1. Magnetic studies

The magnetic hysteresis loop for all the samples was drawn at 300 K and 5 K. The magnetic hysteresis loop of 300 K is shown in Fig. 16. The magnetic hysteresis loop for all the samples shows superparamagnetic and some ferromagnetic nature. The Fe^{3+} ions change to Fe^{4+} ions at the Bi-site with the increasing concentration of divalent Sr^{2+} ions. This substitution introduces some oxygen vacancies to compensate for the charge of the doped samples.[9]

The variation of saturation magnetization and the magnetic moment with Sr content is also plotted and is shown in Fig. 17.

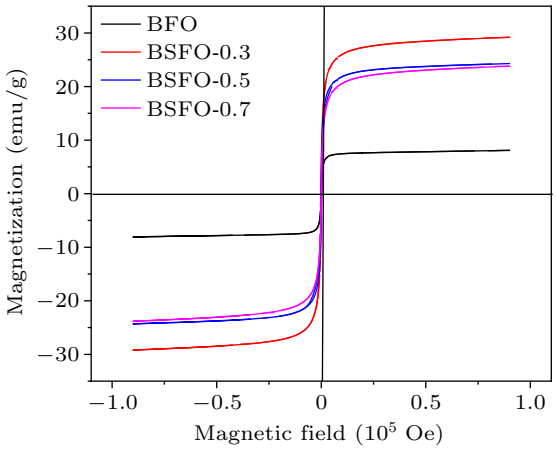


Fig. 16. The M–H loops for the samples at 300 K.

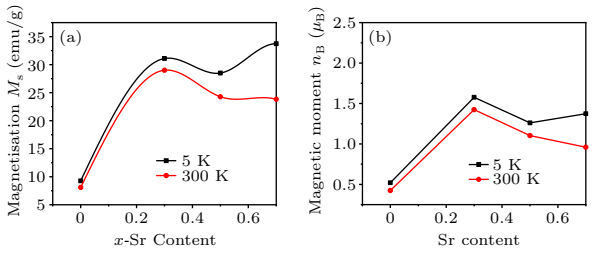


Fig. 17. Magnetization and magnetic moments of all the samples.

Strontium doping at the bismuth site restores its antiferromagnetic behavior and also compresses the spins because of a change in the ionic radius of strontium compared to that of bismuth. This has been reported to result in increased magnetization in Sr-doped BFO.[9] BFO displays a distorted rhombohedral structure and collinear anti-parallel spin arrangement of Fe ions, following zero macroscopic magnetization.[10] Spin canting of magnetic moments at the nanoparticle exterior is the origin of weak ferromagnetism or an (anti) ferromagnetic system. The weak ferromagnetism in BFO ($x = 0$) is due to the spin canting of magnetic moments. For $x = 0.3$ saturation, the magnetization is found to be nearly four times larger than bismuth ferrite. This enhancement of magnetization is explained by the size. The size of the $Bi_{0.7}Sr_{0.3}FeO_3$ nanoparticles is much smaller (10.03 nm) compared to BFO nanoparticles (48.39 nm), which would increase the spin canting of the magnetic moments and hence the Dzyaloshinskii–Moriya (DM) interaction, thus increasing the magnetization. The increase in remnant magnetization (M_r) and the coercive field (H_c) also established the spin canting of the magnetic moments. For $x = 0.5$, a decrease in magnetization is because of the structural transition to the pseudo-cubic (Pm-$3m$) phase. The Fe ions in this structure (Pm-$3m$) are present in an antiparallel collinear configuration with an Fe–O–Fe bond angle of 180° and hence decreased saturation magnetization. For $x = 0.7$, there is also a decrease in magnetization due to the structural transition from the Pm-$3m$ to the Fd-$3m$ phase. The magnetic moment of all the samples is calculated using the equation[10]

$$n_B = \frac{M \cdot M_s}{N_A \cdot \mu_B}, \tag{10}$$

where M is the molecular weight, M_s is the saturation magnetization, and $N_A\mu_B$ is a constant and equal to 5585.

The magnetic coercivity (H_c) of the Bi–Sr ferrite nanoparticles as a function of strontium doping x is shown in Fig. 18. It is seen that initially, with the increase in strontium doping $x = 0.3$, the magnetic coercivity increases from the initial value 24.43 Oe to 70.08 Oe due to the structural transition and then the value decreases for $x = 0.5$ and 0.7. In general, magnetic coercivity depends upon the domain wall energy, magneto-crystalline anisotropic constant, average grain size, and other factors.[39] The initial increasing coercivity value is due to an increase in magneto-crystalline anisotropy. There will be a relation between the anisotropy constant K with the Sr^{2+} ion concentration x, which is calculated using the relation

$$H_C = \frac{0.96K}{M_s}. \tag{11}$$

The calculated anisotropic constant for our samples is listed in Table 3.[40] From the above relation, for greater values of the anisotropy constant and saturation magnetization, the coercivity will also increase. The observed increase in coercivity values is probably due to a decrease in the grain size. For $x = 0.5$ and 0.7, the size increases and the coercivity decreases. The inverse relation between the coercivity and the grain size is reported in the literature.[41]

Table 3. The observed remanent magnetization (M_r), saturation magnetization (M_s), coercive field (H_c), magnetic moment (n_B), M_r/M_S ratio, and anisotropic constant for all the samples at 300 K.

Sr content in sample (x)	M_r (emu/g)	M_s (emu/g)	H_c (Oe)	Magnetic moment n_B (μ_B)	M_r/M_S	K (10^2 erg/g)
0	2.6	7.58	24.43	0.424	0.34	1.92
0.3	3.64	28.76	70.68	1.42	0.12	21.17
0.5	4.84	24.44	24.43	1.10	0.19	6.22
0.7	1.0	23.52	15.24	0.959	0.04	3.73

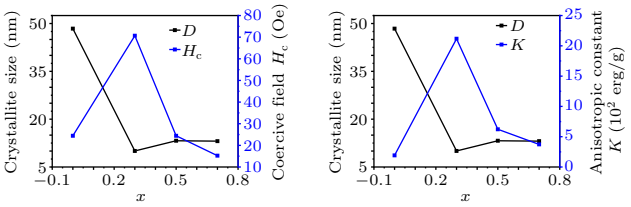


Fig. 18. The variation in crystallite size, coercive field, and anisotropic constant with Sr content in all the samples.

The M_r/M_s, the squareness ratio (SQR), is an important property in memory device applications (~ 1). A small SQR value shows the isotropic nature. The SQR shows how to square the M–H hysteresis loop. In the Stoner–Wohlfarth model, M_r/M_s is 0.34 for BFO nanoparticles and it is in very good agreement with the reported values.[42,43] The low remanent magnetization and coercive field value indicates the superparamagnetic behavior of all the samples. All the samples exhibit a superparamagnetic nature due to suppression of spin cycloid magnetic moments.[43] The observed value of the saturation magnetization of all the samples in the present work is greater than the reported value.[9]

The magnetization measurements were also carried out at a low temperature (5 K). The net value of saturation magnetization is found to increase with a decrease in temperature, which is in agreement with the reported literature and theories.[10,44,45]

5. Conclusion

$BiFeO_3$ and doped samples are successively synthesized using a modified sol-gel auto-combustion process with a crystallite size less than 50 nm. It is a very easy, cost-effective, and less time-consuming process. The XRD pattern that confirms the structural transition from rhombohedral to cubic is found for $x = 0.3$, which confirms the successful replacement of Bi with Sr. The dielectric constant decreases with increasing frequency. The high-value dielectric constant was observed for all the samples, and this will be useful in applications in photoelectrochemical cells and gate dielectrics. The dielectric constant, as well as ac conductivity, can be modified by the addition of dopants. Cole–Cole plots were drawn and various parameters were evaluated. The average relaxation time and molecular relaxation time are calculated and they are approximately the same order ($\sim 10^{-8}$ s). The activation energy of bismuth ferrite is 0.24 eV, which is almost equal to the reported values. The low activation energy of BFO can be used in semiconductor applications. The lower band gap in bismuth ferrite nanoparticles is prepared to indicate that it can be used for multiferroic semiconductors, photocatalytic applications, and hydrogen generation through photocatalytic water splitting. O-vacancy induced strong and sharp photoluminescence activity is observed in the IR region and is useful in optical communication applications, which opens new avenues for the material. The magnetic studies confirm that this is a simple cost-effective method to prepare bismuth ferrite with improved magnetic characteristics. Saturation magnetization and remnant magnetization were found to increase with Sr-content. Magnetic measurements showed that for $x = 0.3$, the saturation magnetization (28.76 emu/g) is nearly four times greater than in BFO (7.58 emu/g), which is due to the spin canting of magnetic moments. The magnetic moment and anisotropic constant are also evaluated. Sr-substituted BFO nanoparticles show superparamagnetic and some ferromagnetic nature; therefore, these materials are promising for future magnetic device applications.

Acknowledgments

Project supported by the Support from DST, Govt of India for the FIST grant sanctioned to Vimala College Thrissur (Grant No. SR/FST/College-046/2011). The authors also thank Dr. M. R Anantharaman, CUSAT for dielectric measurement, and STIC CUSAT for structural characterization. The authors would like to thank Sultan Qaboos University for the support provided during this study.

References

[1] Eerenstein W, Mathur N D and Scott J F 2006 *Nature* **442** 759
[2] Zavaliche F, Zhao T, Zheng H, Straub F, Cruz M P, Yang P L, Hao D and Ramesh R 2007 *Nano Lett.* **7** 1586
[3] Spaldin N A and Fiebig M 2005 *Science* **309** 391
[4] Bhushan B, Basumallick A, Vasanthacharya N Y, Kumar S and Das D 2010 *Solid State Sciences* **12** 1063
[5] Khomchenko V A, Kiselev D A, Selezneva E K, Vieira J M, Lopes A M L, Pogorelov Y G, Araujo J P and Kholkin A L 2008 *Materials Letters* **62** 1927
[6] Soibam I and Devadatta Mani A 2018 *Materials Today: Proceedings* vol. 5 (Elsevier Ltd) pp. 2064–73
[7] Ahlawat A, Satapathy S, Bhartiya S, Singh M K, Choudhary R J and Gupta P K 2014 *Appl. Phys. Lett.* **104** 042902
[8] Costa L V, Ranieri M G, Cilense M, Longo E and Simões A Z 2014 *J. Appl. Phys.* **115** 17D910

[9] Hussain T, Siddiqi S A, Atiq S and Awan M S 2013 *Progress in Natural Science: Materials International* **23** 487

[10] Anju, Agarwal A, Aghamkar P and Lal B 2017 *J. Magn. Magn. Mater.* **426** 800

[11] Van Minh N and Gia Quan N 2011 *J. Alloys Compd.* **509** 2663

[12] Kalyanasundaram K and Grätzel M 1998 1998 *Applications of Functionalized Transition Metal Complexes in Photonic and Optoelectronic Devices* vol. 77

[13] Ma W, Sun Q, Sun M, Bai L, Liu Y, Zhang J and Yang J 2022 *Appl. Surf. Sci.* **571** 151130

[14] Hegab A F, Farag I S A, El-Shabiny A M, Nassaar A M and Ramadan A A 2015 *Journal of Ovonic Research* **11** 235

[15] Razet A 1998 *Metrologia* **35** 143

[16] Jun Y K, Moon W T, Chang C M, Kim H S, Ryu H S, Kim J W, Kim K H and Hong S H 2005 *Solid State Commun.* **135** 133

[17] Singh R and Ulrich R K 1999 *Electrochemical Society Interface* **8** 26

[18] Yadav V S, Sahu D K, Singh Y and Dhubkarya D C 2010 *Proceedings of the International MultiConference of Engineers and Computer Scientists 2010, IMECS* **3** 1593

[19] Veena Gopalan E, Malini K A, Sakthi Kumar D, Yoshida Y, Al-Omari I A, Saravanan S and Anantharaman M R 2009 *J. Phys.: Condens. Matter* **21** 146006

[20] Abo El Ata A M and Attia S M 2003 *J. Magn. Magn. Mater.* **257** 165

[21] Kaur B, Singh L, Annapu Reddy V, Jeong D Y, Dabra N and Hundal J S 2016 *International Journal of Electrochemical Science* **11** 4120

[22] Wang Y P, Zhou L, Zhang M F, Chen X Y, Liu J M and Liu Z G 2004 *Appl. Phys. Lett.* **84** 1731

[23] Mostafa M, Rahman M J and Choudhury S 2019 *Science and Engineering of Composite Materials* **26** 62

[24] Chang F, Zhang N, Yang F, Wang S and Song G 2007 *J. Phys. D: Appl. Phys.* **40** 7799

[25] Daniel V 1967 *Dielectric relaxation* (New York: Academic Press)

[26] Hill N E 1969 *Dielectric properties and molecular behaviour* (eBook)

[27] Sagar S, Saravanan S, Suresh Kumar S, Venkatachalam S and Anantharaman M R 2006 *J. Phys. D: Appl. Phys.* **39** 1678

[28] Rayssi C, El Kossi S, Dhahri J and Khirouni K 2018 *RSC Advances* **8** 17139

[29] Chawla M, Shekhawat N, Aggarwal S, Sharma A and Nair K G M 2014 *J. Appl. Phys.* **115** 184104

[30] Chaudhuri A and Mandal K 2014 *JJ. Magn. Magn. Mater.* **353** 57

[31] Rao T D, Karthik T and Asthana S 2013 *Journal of Rare Earths* **31** 370

[32] Francis P N, Dhanuskodi S, Jayalakshmy M S, Muneeswaran M, Philip J and Giridharan N V 2018 *Materials Chemistry and Physics* **216** 93

[33] Kaur B, Singh L, Annapu Reddy V, Jeong D Y, Dabra N and Hundal J S 2016 *International Journal of Electrochemical Science* **11** 4120

[34] Li Z, Shen Y, Yang C, Lei Y, Guan Y, Lin Y, Liu D and Nan C W 2013 *Journal of Materials Chemistry A* **1** 823

[35] McDonnell K, Wadnerkar N, English N J, Rahman M and Dowling D 2013 *Chemical Physics Letters* **572** 78

[36] Deng J, Banerjee S, Mohapatra S K, Smith Y R and Misra M 2011 *Journal of Fundamentals of Renewable Energy and Applications* **1** 1

[37] Boccuzzi F, Ghiotti G, Chiorino A and Marchese L 1990 *Surface Science* **233** 141

[38] Reddy A J, Kokila M K, Nagabhushana H, Chakradhar R P S, Shivakumara C, Rao J L and Nagabhushana B M 2011 *J. Alloys Compd.* **509** 5349

[39] Kurmude D V., Kale C M, Aghav P S, Shengule D R and Jadhav K M 2014 *Journal of Superconductivity and Novel Magnetism* **27** 1889

[40] Kambale R C, Song K M, Koo Y S and Hur N 2011 *J. Appl. Phys.* **110** 053910

[41] Gabal M A, El-Shishtawy R M and Al Angari Y M 2012 *J. Magn. Magn. Mater.* **324** 2258

[42] Rhaman M M, Matin M A, Hossain M N, Khan M N I, Hakim M A and Islam M F 2020 *Journal of Physics and Chemistry of Solids* **147** 109607

[43] Sarkar K, Mukherjee S and Mukherjee S 2015 *Processing and Application of Ceramics* **9** 53

[44] Yang C, Han Y, Qian J, Lv P, Lin X, Huang S and Cheng Z 2019 *ACS Applied Materials and Interfaces* **11** 12647

[45] Yang C, Qian J, Lv P, Wu H, Lin X, Wang K, Ouyang J, Huang S, Cheng X and Cheng Z 2020 *Journal of Materiomics* **6** 200